Numerical Simulation of Wave Impacts with Interfacial Phase Change: An Interface Reconstruction Scheme

Matthieu Ancellin, Laurent Brosset, Jean-Michel Ghidaglia

Numerical Simulation of Wave Impacts with Interfacial Phase Change: An Interface Reconstruction Scheme

Matthieu Ancellin[a,b,*], Laurent Brosset[a], Jean-Michel Ghidaglia[b]

[a] *GTT (Gaztransport & Technigaz), Saint-Rémy-lès-Chevreuse, France*
[b] *CMLA, ENS Paris-Saclay, CNRS, Université Paris-Saclay, Cachan, France*

Abstract

Most current numerical simulations on sloshing impact loads do not take into account the possibility of evaporation and condensation of the fluid. Our goal is to develop a numerical model able to simulate a wave impact with phase change in order to evaluate the influence of phase change on sloshing impact loads. The proposed model describes compressible multiphase flows with separate phases and non-equilibrium interfacial phase change. In this paper, the liquid-vapor interface is discretized using the interface reconstruction scheme of [1]. Implementation of a phase change model in such a framework is presented. In particular, the agreement of the model with the Second Law of Thermodynamics is discussed. The discretized model is first tested using simple return to equilibrium test cases. Then the model is applied to the one-dimensional piston problem that models the behavior of a compressed gas pocket during a breaking wave impact.

1. Introduction

Currently, one of the main technologies used to store and transport Liquefied Natural Gas (LNG) is a membrane containment system, which keeps LNG at ambient pressure and cryogenic temperatures. However, the motion of the ship may cause significant movement of the tank liquid, which can induce violent

*Corresponding author
Email addresses: matthieu.ancellin@cmla.ens-cachan.fr (Matthieu Ancellin), lbrosset@gtt.fr (Laurent Brosset), jmg@cmla.ens-cachan.fr (Jean-Michel Ghidaglia)

impacts on the containment system. To ensure that the design of such a containment system is safe, Gaztransport & Technigaz (GTT) has to ensure that no damage is caused by these impacts during the working life of the floating structure. Sloshing assessment is usually based on small scale tests (typically at scale 1:40) using a model tank filled with water and a heavy gas (keeping the same gas-to-liquid density ratio) placed on a six degrees of freedom hexapod platform. Impact pressure is measured by many sensors placed in the impact areas. The probability of failure for any limit state of the containment system is then derived using a complex methodology based on a long-term approach [2].

However, some of the physical aspects found in real wave impacts are not captured in these small scale experiments. In this work we are particularly interested in the change of phase (evaporation and condensation) that could occur in the LNG when the liquid is in thermodynamic equilibrium with its gaseous phase. This paper is part of a series of articles dedicated to the numerical simulation of wave impacts with phase change, where further understanding is sought on the role of phase change in LNG tank sloshing impacts.

Sloshing tests have been performed with boiling water and vapor in conditions close to the phase boundary [3]. The pressure at the impact wall was found to be statistically smaller with water and vapor than with water and non-condensible gases. This pressure reduction has been attributed to phase change. Moreover, at each time a vapor pocket was entrapped between the liquid and the wall, pressure oscillations that are typically observed with non-condensible gases were absent. The vapor pockets seemed to behave like punctured balls without any stiffness.

Simulating a wave impact with phase change adds a new layer of difficulty to an already complex problem, since the numerical model with phase change should already include complex properties of the two fluids, for example their compressibility [4, 5]. Furthermore, it is impossible to directly validate such simulations because experimental results of wave impact tests (or sloshing tests with a single impact) show a high variability in local pressure measurements.

This variability is due to the development of free surface instabilities triggered by the escaping gas flow, even when the global wave shape is accurately reproduced. The surface tension that drives these instabilities is often neglected in state-of-the-art works on wave impacts. Its modelisation is out of the scope of this paper. More details on the physics of wave impacts can be found in [6].

Among the several numerical methods used in the last years for the simulation of wave impacts, this paper will focus in particular on the Finite Volume method for two non-miscible compressible fluids of Braeunig et al. [1, 7]. It has been applied to the simulation of an idealized wave impacts problem [4] in a benchmark study organized within the ISOPE conferences in 2010 and 2013. Since then, several improvements have been made in the code [8, 9, 10, 11] and other applications to wave impacts without phase change have been presented [12, 13]. The main advantages of this code for the simulation of wave impacts are its ability to model two compressible phases with any equation of state and its sharp representation of the interface limiting the mitigation due to numerical diffusion. The goal of the present work is the introduction of phase change in these simulations.

The only other attempts (to our knowledge) to simulate an impact with phase change have been made by [14] for the idealized scenario of [4] and by [15] for two single impact waves obtained by sloshing model tests (without experiment as a reference). Their results seem to be in line with those observed by [3] for sloshing tests with boiling water and vapor, assuming the thermodynamical equilibrium at any time.

An isothermal Volume-Of-Fluid-type model for the simulation of impacts with phase change has been presented in [16, 17]. Preliminary results show an increase in pressure at the wall: when phase change occurs, vapor contained in the gas cushion between the liquid and the wall condenses and does not slow down the liquid motion. However, this result has several shortcomings, mainly concerning the isothermal hypothesis, which will be removed in the present paper.

The present question on the role of phase change in sloshing wave impacts is related to the problem of the influence of sloshing on boil-off evaporation in cryogenic tanks. The contents of a cryogenic tank is slowly warmed by steady heat flow passing through the tank walls, thus leading to some liquid evaporation. This phenomenon is affected by the motion of the tank, as discussed in e.g. [14]. The spatial scale of this problem is the size of the tank and the time scale is hours or days. However, the spatial scale of our problem is a single impact and its time scale is the duration of the impact. These two problems thus require different modeling approaches.

References in the literature involving phase change are numerous and diverse. (The reader is referred to [18] and [19], for instance.) The two-phase CFD models can be sorted by the characteristic size and duration of the studied problem.

A microscopic problem would involve a liquid-vapor interface described as an intermediate zone of finite thickness (e.g. [20]). At a larger scale, the interface would be represented as a sharp discontinuity between two pure phases (e.g. [21] and [22]). For complex flows, the location of the interface would be averaged in a mixture model, such as the one described in [23]. Different interface models require different phase change modeling.

For the description of wave impacts, the interface is usually modeled as a sharp discontinuity between two pure phases (as in [4]). The possibility of a complex flow involving bubbles and droplets caused by free surface instabilities is then neglected for the sake of simplicity. This same hypothesis will be made in this paper.

Typical models for slow evaporation and condensation are based on the Stefan model [24]. In such a model, the mass flow rate can be seen as a Lagrange multiplier ensuring the instantaneous equilibrium condition $p = p^{\mathrm{sat}}(T)$ at the interface. However, a wave impact is a very brief and violent phenomenon and it is undesirable to make an equilibrium hypothesis at the interface. Instead, the mass flow rate will be derived in the framework of *linear non-equilibrium*

thermodynamics. The main reference on this topic is [25]. We will also refer the reader to [26], [27] and [28] for an application of this framework to liquid-vapor interfaces.

In this paper, only phase change at the interface between liquid and gas is discussed. We do not expect nucleation, which is the appearance of new droplets in the gas or new bubbles in the liquid, to be necessary for the understanding of the influence of phase change on wave impacts [16, 29].

The numerical simulation of liquid-vapor phase change presents several challenges. First, the low gas-to-liquid density ratio causes a velocity discontinuity at the interface (due to conservation of the mass flux ρu). Fluid that is changing phase needs to contract or expand to adjust to its new density, which leads to pressure variations. Moreover, the latent heat released or captured during phase change can lead to large variations in temperature around the interface, as also discussed in [30], which means that the resolution of the heat diffusion equation cannot be completely decoupled from the rest of our study. Rigorous integration of all of this phenomena into a numerical code is a difficult task. The main goal of this paper is to present and validate our solutions to these challenges.

In the next section, mathematical equations that describe two-phase flow with non-equilibrium phase change are presented. Emphasis is placed on the evaluation of phase change mass and energy fluxes that are compliant with the Second Principle of Thermodynamics.

In the following section, the equations have been discretized using a Finite Volume framework with the interface capturing Roe-type scheme of [1]. Again the fulfillment of the Second Principle of Thermodynamics is discussed, this time in a discrete framework.

Finally some numerical results are presented. First, a simple return to equilibrium test case is discussed. Then the code is applied to the one-dimensional piston problem [31], which models a simple wave impact that forms a gas pocket. The code will be validated by comparison with the surrogate models of [32, 16].

The present work is part of a series on the modeling of wave impacts with phase change. It has been presented in [16] along with a diffuse interface model (presented in [17]) and a surrogate model that is an update of the model presented in [32]. These different works explore different approaches and shed light on different aspects of phase change modeling. A summary of the models and partial physical conclusions are presented in [33].

2. Physical model

In this section a mathematical description of a two-fluid flow with interfacial phase change will be discussed. Only the one-dimensional case will be discussed in this paper.

2.1. Eulerian model

The two phases are described with the help of an order parameter $\chi(x,t)$ associated with the local phase ($\chi = 1$ for the gas and $\chi = 0$ for the liquid). When there is no phase change this parameter is simply advected by the material velocity of the fluid. However, occurrence of phase change means that χ changes, even when both fluids are at rest. Let us denote ω as the evolution velocity of the liquid-vapor interface, that is

$$\partial_t \chi + \omega \partial_x \chi = 0. \tag{1}$$

By integrating the mass conservation equation around the interface, ω can be linked to the mass flow rate across the interface [16]. Then (1) can be rewritten as

$$\partial_t \chi + \left(u - \frac{J}{\rho} \right) \partial_x \chi = 0, \tag{2}$$

where J denotes the interfacial surface mass flux, which is positive in the left to the right direction. The mass flux J can be related to the evaporation mass flux $J_{l\to g}$ (positive from liquid to gas) by

$$J = \begin{cases} J_{l\to g} & \text{if the liquid is on the left and the gas on the right,} \\ -J_{l\to g} & \text{if the gas is on the left and the liquid on the right.} \end{cases}$$

This equation can be combined with the usual compressible Euler conservation equations, as follows:

$$\partial_t \rho + \partial_x(\rho u) = 0, \tag{3a}$$

$$\partial_t(\rho u) + \partial_x(\rho u \otimes u + p\,\mathbb{I}) = 0, \tag{3b}$$

$$\partial_t\left(\rho E\right) + \partial_x\left(\left(\rho E + p\right) u + q\right) = 0, \tag{3c}$$

$$\partial_t(\chi\rho) + \partial_x(\chi\rho u) - J\partial_x\chi = 0, \tag{3d}$$

where ρ, u, p, and $E = e + |u|^2/2$ denote respectively the density, the velocity, the pressure and the specific total energy of the fluid. Equation (3d) has been obtained by combining (2) with (3a).

The diffusive heat flux q is given in general by Fourier's law. As mentioned in [30], the problem is not physically meaningful without heat conduction. Indeed, the latent heat for steam and water (or methane and liquid methane) is relatively high and thus significant temperature gradients might appear near the interface.

More terms can be added on the right-hand side of (3) to describe, for instance, gravity, inertial accelerations or molecular diffusion. In this paper, we focus only on the hyperbolic part of the equations (including the phase change term $J\partial_x\chi$).

2.2. Lagrangian form

The numerical scheme used for simulation of (3) can be derived from the Lagrangian form of the conservation equations, as we will see in Section 3.2. The balance laws (3) can be rewritten in the following Lagrangian form:

$$\mathrm{d}_t^u \tau - \partial_x u = 0, \tag{4a}$$

$$\mathrm{d}_t^u u + \partial_x p = 0, \tag{4b}$$

$$\mathrm{d}_t^u E + \partial_x(p\,u) = -\partial_x q, \tag{4c}$$

$$\mathrm{d}_t^u \chi - J\partial_x\chi = 0, \tag{4d}$$

where $\tau = 1/\rho$ is the specific volume and

$$\mathrm{d}_t^u = \rho\partial_t + \rho u \cdot \partial_x \tag{5}$$

is the material time derivative in the frame of the fluid, moving at velocity u.

However, the velocity of interface ω is in general different from the material velocity u. In the reference frame of the interface, moving at velocity ω, these equations can be rewritten as

$$\mathrm{d}_t^\omega \tau - \partial_x u + J\partial_x \tau = 0, \tag{6a}$$

$$\mathrm{d}_t^\omega u + \partial_x p + J\partial_x u = 0, \tag{6b}$$

$$\mathrm{d}_t^\omega E + \partial_x pu + J\partial_x E = -\partial_x q, \tag{6c}$$

$$\mathrm{d}_t^\omega \chi = 0, \tag{6d}$$

with

$$\mathrm{d}_t^\omega = \rho\partial_t + \rho\omega \cdot \partial_x. \tag{7}$$

The non-conservative terms in (6) correspond to the flow of volume, momentum and energy exchanged during phase change. Without phase change $\omega = u$ and $J = 0$, and thus the usual Euler equations in Lagrangian form are retrieved.

The boundary conditions at the interface (such as the velocity jump and the pressure jump [34]) are implicitly included in the conservation equations (3) or (6). They are not explicitly implemented in the code but will be fulfilled as a consequence of the fulfillment of the discrete conservation laws.

2.3. Mass flux and entropy balance

We have introduced one more variable J in the equations, thus it is necessary to have one more relation to close the system. This will take the form of a kinetic relation between J and the local thermodynamical state near the interface. In this section, we will derive such a relation for J that is consistent with the Second Principle of Thermodynamics.

The entropy balance across the interface (see [16] or [34]) reads

$$J_{l\to g}(s_g - s_l) + \left(\frac{q_g}{T_g} - \frac{q_l}{T_l}\right) \cdot \nu_{l\to g} \geq 0\,, \tag{8}$$

where $J_{l\to g}$ is the evaporation mass flux, s_g, s_l, T_g, T_l, q_g and q_l are the entropy, temperature and heat flux respectively on the gas side and liquid side

of the interface, and $\nu_{l\to g}$ is the unit normal vector oriented from the liquid side to the gas side of the interface.

Using the energy jump condition across the interface, we can introduce the total energy flux across the interface as

$$\begin{aligned} Q_{l\to g} &= J_{l\to g}\left(h_g + \frac{|u_g-\omega|^2}{2}\right) + q_g\cdot\nu_{l\to g}, \\ &= J_{l\to g}\left(h_l + \frac{|u_l-\omega|^2}{2}\right) + q_l\cdot\nu_{l\to g}, \end{aligned} \tag{9}$$

where u_g, u_l, h_g and h_l denote respectively the velocity and the specific enthalpy on the gas and liquid sides. With this relation, the entropy condition (8) can be rewritten as

$$-J_{l\to g}\left(\frac{\mu_g + \frac{1}{2}|u_g-\omega|^2}{T_g} - \frac{\mu_l + \frac{1}{2}|u_l-\omega|^2}{T_l}\right) + Q_{l\to g}\left(\frac{1}{T_g}-\frac{1}{T_l}\right) \geq 0, \tag{10}$$

where μ_g and μ_l are the chemical potentials of the gas and the liquid. For a pure species the chemical potential is identical to the specific free enthalpy $g = h - Ts$. Both magnitudes will not be distinguished in this paper.

We assume the existence of relations between the flux and the local states near the interface:

$$Q_{l\to g} = \mathcal{Q}_{l\to g}(p_l, T_l, p_g, T_g), \qquad J_{l\to g} = \mathcal{J}_{l\to g}(p_l, T_l, p_g, T_g). \tag{11}$$

The closure relations $\mathcal{Q}_{l\to g}$ and $\mathcal{J}_{l\to g}$ will be expressed in the framework of linear non-equilibrium thermodynamics. (The reader is referred to [26], [27] and [28] for an application of this framework to liquid-vapor interfaces.) The main philosophy of this approach is to assume that a flux is proportional to a measure of the corresponding non-equilibrium. The entropy creation rate will be used to identify pairs of flux and non-equilibrium. Thus ensuring fulfillment of the Second Principle of Thermodynamics.

Close to equilibrium and for small mass flux $J_{l\to g}$, it can be shown [16] that the closure relations

$$Q_{l\to g} = G_q(T_l - T_g) + h_g(p_g, T_g)J_{l\to g}, \qquad J_{l\to g} = G_m\frac{\mu_l(p_l,T_l) - \mu_g(p_g,T_l)}{T_l}, \tag{12}$$

where $G_m \geq 0$ and $G_q \geq 0$ are constant relaxation rates, respect the entropy condition (10).

Note that relation (12) could have been written symmetrically for the liquid instead of the gas as

$$Q_{l\to g} = G_q(T_l - T_g) + h_l(p_l, T_l)J_{l\to g}, \qquad J_{l\to g} = G_m \frac{\mu_l(p_l, T_g) - \mu_g(p_g, T_g)}{T_g}, \tag{13}$$

The choice of such an asymmetry is based of physical hypotheses. Considering that the liquid has a larger thermal diffusivity coefficient than the gas, it is often assumed that phase change at the interface occurs at temperature T_l. This is implicitly stated by (12): the phase change non-equilibrium measure $\mu_l - \mu_g$ is evaluated at T_l. However, it could be evaluated at any temperature (such as T_g in (13)), the Second Principle only imposes that a corresponding expression for $Q_{l\to g}$ has to be chosen.

The mass flux from (12) can be linearized [16] to retrieve an expression close to the well-known Hertz-Knudsen relation:

$$Q_{l\to g} = G_q(T_l - T_g) + h_g(p_g, T_g)J_{l\to g}, \qquad J_{l\to g} = -G_m \frac{\tau_g(p^{\mathrm{sat}}(T_l), T_l)}{T_l}\big(p_g - p^{\mathrm{sat}}(T_l)\big). \tag{14}$$

3. Discretization

The model will be discretized using the FVCF-IC scheme that is presented in this section. We refer to [1] [7], or [9] for full details. Note that a similar strategy could be applied to other types of Arbitrary Lagrangian-Eulerian schemes to model phase change.

3.1. Scheme without phase change

3.1.1. Presentation

Figure 1 presents the different steps in the management of an interface by the code. First, the mixed cells and the neighboring cells are fused into a set of layers of pure fluid called *condensate* during the reconstruction step. These

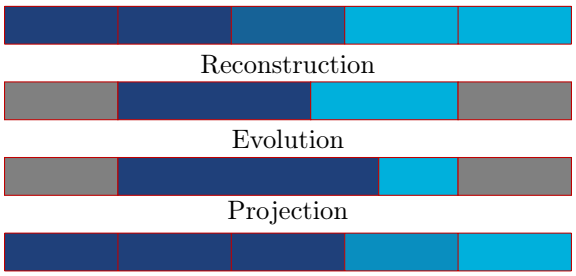

Figure 1: Diagram of the different steps of the scheme in 1D for a simple condensate (with two layers).

layers evolve according Lagrangian principles during a time step Δt. Finally, the condensate is projected onto the initial Cartesian mesh. The rest of the domain is resolved using an usual Finite Volume scheme in the Eulerian framework.

The word *condensate* has been introduced by [7] to denote layers of liquid and gas without phase change. In this work, this work will be extended to include phase change and thus the word condensate could instead refer to the fluid having changed phase from gas to liquid. However, we have chosen to keep the wording of [7] in this paper: *condensate* will always denote layers of liquid and gas disregarding whether phase change is happening or not.

The scheme can be extended to higher dimensions using a directional time splitting approach. The reconstruction and projection phases in higher dimensions are independent of phase change modeling and thus they will not be discussed here, and instead we refer the reader to the previously cited works.

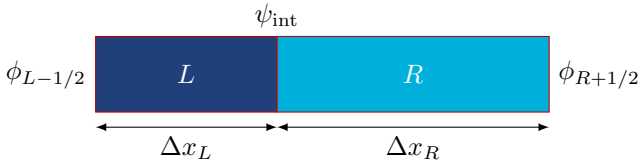

Figure 2: Notation for a simple condensate

The numerical evolution of the interface can be expressed using the La-

grangian formalism of the Euler evolution equation

$$\mathrm{d}_t^u v + \partial_x F = 0, \tag{15}$$

where

$$v = \begin{pmatrix} \tau \\ u \\ E \end{pmatrix}, \qquad F = \begin{pmatrix} -u \\ p \\ pu \end{pmatrix},$$

The numerical flux approximating F at the Lagrangian interface is written in the form:

$$\psi_{\text{int}} = \begin{pmatrix} -u_{\text{int}} \\ p_{\text{int}} \\ u_{\text{int}} p_{\text{int}} \end{pmatrix}. \tag{16}$$

where

$$u_{\text{int}} = \frac{\rho_L c_L\, u_L + \rho_R c_R\, u_R}{\rho_L c_L + \rho_R c_R} + \frac{p_L - p_R}{\rho_L c_L + \rho_R c_R}, \tag{17a}$$

$$p_{\text{int}} = \frac{\rho_L c_L\, p_L + \rho_R c_R\, p_R}{\rho_L c_L + \rho_R c_R} + \rho_L c_L\, \rho_R c_R \frac{u_L - u_R}{\rho_L c_L + \rho_R c_R}. \tag{17b}$$

Subscripts L and R respectively denote left and right as presented in Figure 2.

Besides, the flux at the exterior boundaries of the condensate is expressed with the usual numerical flux in the Eulerian framework:

$$\phi_{L-1/2} = \phi(v_{L-1}, v_L), \qquad \phi_{R+1/2} = \phi(v_R, v_{R+1}).$$

Finally, the fluxes will be used to update the volume, mass, momentum and total energy of each layer of the condensate:

$$\Delta x_L^{n+1} = \Delta x_L^n - \Delta t\, \psi_{\text{int}}^{\tau}, \tag{18a}$$

$$(\Delta x \rho)_L^{n+1} = (\Delta x \rho)_L^n + \Delta t\, \phi_{L-1/2}^{\rho}\,, \tag{18b}$$

$$(\Delta x \rho u)_L^{n+1} = (\Delta x \rho u)_L^n - \Delta t \left[\psi_{\text{int}}^{u} - \phi_{L-1/2}^{\rho u}\right], \tag{18c}$$

$$(\Delta x \rho E)_L^{n+1} = (\Delta x \rho E)_L^n - \Delta t \left[\psi_{\text{int}}^{E} - \phi_{L-1/2}^{\rho E}\right], \tag{18d}$$

and similarly for the right hand side R. In the above equation, ψ^{τ} denotes the component of the Lagrangian flux describing the variation of specific volume, ϕ^{ρ} denotes the component of the Eulerian flux describing the variation of volumic mass, and so on.

3.1.2. Entropy balance

We now check that the numerical flux (16) fulfills the Second Principle of Thermodynamics. This result is analogous to Proposition 11 of [7] with a slightly different discrete entropy condition.

The physical entropy condition can be rewritten with the help of the system of conservation laws (15) as:

$$0 \leq \mathrm{d}_t^u s = \frac{\partial s}{\partial v} \mathrm{d}_t^u v = -\frac{\partial s}{\partial v} \partial_x F.$$

It can thus be integrated in the neighborhood of an interface as follows:

$$-\int_L^R \frac{\partial s}{\partial v} \partial_x F \mathrm{d}x \simeq \left(\frac{\partial s}{\partial v}\right)_L (F_L - \psi_{\mathrm{int}}) + \left(\frac{\partial s}{\partial v}\right)_R (\psi_{\mathrm{int}} - F_R). \tag{19}$$

Using the fact that

$$\frac{\partial s}{\partial v} = \frac{1}{T} \begin{pmatrix} p \\ -u \\ 1 \end{pmatrix},$$

we can check that the numerical flux (16) is entropic in the sense of

$$\left(\frac{\partial s}{\partial v}\right)_L (F_L - \psi_{\mathrm{int}}) + \left(\frac{\partial s}{\partial v}\right)_R (\psi_{\mathrm{int}} - F_R) \geq 0.$$

3.2. Scheme with phase change

3.2.1. Presentation

In the following, an extension of this scheme for the simulation of phase change at the interface will be proposed. For this, we will use the "upwind-l" FVCF scheme, as defined in [16] and [17]. It is a variant of the FVCF scheme presented in [35].

Let us notice that the magnitudes of (17) can be seen as the numerical flux for the isentropic Euler equations in Lagrangian form:

$$\mathrm{d}_t^u v + \partial_x F = 0, \tag{20}$$

where

$$v = \begin{pmatrix} \tau \\ u \end{pmatrix}, \qquad F = \begin{pmatrix} -u \\ p \end{pmatrix}.$$

when they are discretized with the "upwind-l" FVCF scheme. It is proposed that phase change is included in the simulation by computing the numerical flux associated with system (6) using the same numerical method.

The non-conservative terms that include the mass flow J will be approximated by a constant value around the interface, which gives the following approximate conservative system:

$$\mathrm{d}_t^\omega \tau + \partial_x(-u + J_{\mathrm{int}}\tau) = 0, \tag{21a}$$

$$\mathrm{d}_t^\omega u + \partial_x(p + J_{\mathrm{int}}u) = 0, \tag{21b}$$

$$\mathrm{d}_t^\omega E + \partial_x(pu + J_{\mathrm{int}}E) = 0, \tag{21c}$$

$$\mathrm{d}_t^\omega \chi = 0. \tag{21d}$$

For instance, with the formalism of (11), J_{int} might read

$$J_{\mathrm{int}} = \begin{cases} \mathcal{J}_{l\to g}\left(p_L, T_L, p_R, T_R\right) & \text{if the liquid is on the left,} \\ -\mathcal{J}_{l\to g}\left(p_R, T_R, p_L, T_L\right) & \text{if the gas is on the left.} \end{cases}$$

For readability, the approximate flux J_{int} will be written as J in the following.

System (21) can be written as the following system of conservation laws

$$\mathrm{d}_t v + \partial_x(F + G) = 0,$$

where

$$v = \begin{pmatrix} \tau \\ u \\ E \\ \chi \end{pmatrix}, \qquad F = \begin{pmatrix} -u \\ p \\ pu \\ 0 \end{pmatrix}, \qquad G = J \begin{pmatrix} \tau \\ u \\ E \\ 0 \end{pmatrix}.$$

The associated Jacobian matrix reads

$$A = \frac{\partial(F+G)}{\partial v} = \begin{pmatrix} J & -1 & 0 & 0 \\ p\rho\Gamma - \rho^2 c^2 & -\rho u\Gamma + J & \rho\Gamma & \rho p_\chi \\ u(p\rho\Gamma + \rho^2 c^2) & p - \rho u^2\Gamma & \rho u\Gamma + J & \rho u p_\chi \\ 0 & 0 & 0 & 0 \end{pmatrix}, \tag{22}$$

where c is the speed of sound, Γ is the Grüneisen coefficient and p_χ is defined as

$$p_\chi = \frac{1}{\rho}\left(\frac{\partial p}{\partial \chi}\right)_{\rho,e}.$$

With the help of symbolic computation software, the eigenvalues and eigenvectors of this system can be computed. The eigenvalues are $J-\rho c$, J, 0, $J+\rho c$, which are respectively associated with the left sonic wave, the contact discontinuity, the phase change interface and the right sonic wave.

The right eigenvectors are:

$$R = \begin{pmatrix} \frac{1}{\rho c} & 1 & p_\chi & -\frac{1}{\rho c} \\ 1 & 0 & Jp_\chi & 1 \\ u-\frac{p}{\rho c} & \frac{\rho c^2}{\Gamma}-p & (Ju-p)p_\chi & u+\frac{p}{\rho c} \\ 0 & 0 & \rho^2c^2-J^2 & 0 \end{pmatrix}. \tag{23}$$

The associated left eigenvectors are:

$$L = \begin{pmatrix} \frac{1}{2}\left(\rho c-\frac{p\Gamma}{c}\right) & \frac{1}{2}\left(1+\frac{u\Gamma}{c}\right) & -\frac{1}{2}\frac{\Gamma}{c} & \frac{1}{2}p_\chi\frac{1}{\rho c-J} \\ \frac{p\Gamma}{\rho c^2} & -\frac{u\Gamma}{\rho c^2} & \frac{\Gamma}{\rho c^2} & 0 \\ 0 & 0 & 0 & \frac{1}{\rho^2c^2-J^2} \\ -\frac{1}{2}\left(\rho c-\frac{p\Gamma}{c}\right) & \frac{1}{2}\left(1-\frac{u\Gamma}{c}\right) & \frac{1}{2}\frac{\Gamma}{c} & \frac{1}{2}p_\chi\frac{1}{\rho c+J} \end{pmatrix}. \tag{24}$$

The Lagrangian numerical flux can then be computed as

$$\psi_{\text{int}}(v_L, v_R) = \frac{F_L+G_L+F_R+G_R}{2} + \operatorname{sgn}\left(\widetilde{A}(v_L,v_R)\right)\frac{F_L+G_L-F_R-G_R}{2} \tag{25}$$

where $\tilde{A}$ is the upwinding matrix approximating A as defined in [16] and [17]. The sign matrix of a matrix $A = L\,\mathrm{diag}(\lambda_j)\,R$ is defined as the matrix $\mathrm{sgn}(A) = L\,\mathrm{diag}(\mathrm{sgn}(\lambda_j))\,R$. The above definition of ψ may be ambiguous when $J=0$, but in this case the flux (16) can be used.

To describe heat exchange between two layers of the condensate, a heat flux term q_{int} can be added to ψ_{int}. It will be seen in the next section that this could be necessary for the entropy condition in the case of phase change.

In the same way as for (18), the scheme reads

$$\Delta x_L^{n+1} = \Delta x_L^n - \Delta t\, \psi_{\text{int}}^\tau, \tag{26a}$$

$$(\Delta x\rho)_L^{n+1} = (\Delta x\rho)_L^n - \Delta t \left[J - \phi^\rho_{L-1/2}\right], \tag{26b}$$

$$(\Delta x\rho u)_L^{n+1} = (\Delta x\rho u)_L^n - \Delta t \left[\psi^u_{\text{int}} - \phi^{\rho u}_{L-1/2}\right], \tag{26c}$$

$$(\Delta x\rho E)_L^{n+1} = (\Delta x\rho E)_L^n - \Delta t \left[\psi^E_{\text{int}} - \phi^{\rho E}_{L-1/2}\right], \tag{26d}$$

and symmetrically for the right hand side cell R. By construction, we have $\chi_L^{n+1} = \chi_L^n$ and $\chi_R^{n+1} = \chi_R^n$.

3.2.2. Entropy balance

In this section, a discrete entropy balance will be written to validate the fulfillment of the Second Principle of Thermodynamics by J. The scheme we propose here does not allow an easy study of this entropy balance as in Section 3.1.2. Nonetheless, an expression for J can be proposed by studying the entropy balance in a particular case in which only the phase change plays a role.

Let us suppose

$$p_L = p_R = p, \qquad u_L = u_R = 0. \tag{27}$$

The numerical flux ψ_{int} satisfies

$$\left(\frac{\partial s}{\partial v}\right)_L (F_L + G_L - \psi_{\text{int}}) + \left(\frac{\partial s}{\partial v}\right)_R (\psi_{\text{int}} - F_R - G_R) = J\frac{h_L - h_R}{T_K},$$

where

$$T_K = \begin{cases} T_L & \text{if } J < 0, \\ T_R & \text{if } J > 0. \end{cases}$$

Following the example of Section 3.1.2, the entropy condition is:

$$\begin{aligned} 0 \leq \mathrm{d}_t^u s &= (\mathrm{d}_t^\omega s - \rho(\omega - u)\partial_x s) \\ &= \frac{\partial s}{\partial v}\mathrm{d}_t^\omega v + J\partial_x s \\ &= -\frac{\partial s}{\partial v}\partial_x(F + G) + J\partial_x s. \end{aligned}$$

This can be discretized in the form of

$$\begin{aligned}&\int_L^R \left(-\frac{\partial s}{\partial v}\partial_x(F+G)+J\partial_x s\right)\mathrm{d}x \simeq \\ &\left(\frac{\partial s}{\partial v}\right)_L (F_L+G_L-\psi_{\text{int}})+\left(\frac{\partial s}{\partial v}\right)_R (\psi_{\text{int}}-F_R-G_R)+J\left(s_R-s_L\right).\end{aligned} \tag{28}$$

With hypothesis (27), the discrete entropy condition (28) is

$$J_{l\to g}\left(s_g-s_l+\frac{h_l-h_g}{T_k}\right)\geq 0, \tag{29}$$

where

$$T_k=\begin{cases}T_g & \text{if } J_{l\to g}<0,\\ T_l & \text{if } J_{l\to g}>0.\end{cases}$$

Let us compare (29) with the entropy balance in Section 2.3. The latter can be rewritten as

$$J_{l\to g}(s_l-s_g)+\frac{J_{l\to g}h_l-Q_{l\to g}}{T_l}-\frac{J_{l\to g}h_g-Q_{l\to g}}{T_g}\geq 0.$$

The term with the enthalpies in (29) can be understood as the entropy creation term for an energy flux of the form

$$Q_{l\to g}^{\text{scheme}}=\begin{cases}J_{l\to g}h_l & \text{if } J_{l\to g}<0,\\ J_{l\to g}h_g & \text{if } J_{l\to g}>0.\end{cases}$$

This energy flux at the interface depends on the sign of the mass flux, which is a natural consequence of the use of an upwind scheme. However, we assumed in (12) that the exchanged enthalpy is the one of the gas. The expression of the heat flux should be adapted to compensate this numerical artifact. The flux

$$q_{\text{int}}=\begin{cases}J_{l\to g}(h_l-h_g) & \text{if } J_{l\to g}<0,\\ 0 & \text{if } J_{l\to g}>0.\end{cases}\qquad J_{l\to g}=G_m\frac{\mu_l(p_l,T_l)-\mu_g(p_g,T_l)}{T_l}, \tag{30}$$

with $G_m\geq 0$, respects the discrete entropy condition. Indeed, it is equivalent to (12) with $\mathcal{Q}_{l\to g}=\mathcal{Q}_{l\to g}^{\text{scheme}}+q_{\text{int}}$ and $G_q=0$.

In the following section, the return to equilibrium test case will allow numerical validation of this result.

4. Validation test case: return to equilibrium

In this section, several variants of the same test case will be presented. We will study how a liquid-vapor interface that is initially out of equilibrium returns to liquid-vapor equilibrium. A similar problem has been presented in [17] with an isothermal hypothesis. We will see here that temperature gradient and heat diffusion play a major role in the relaxation.

4.1. Description

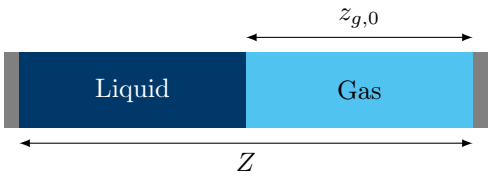

Figure 3: Initial conditions of the test case.

We consider a tube of section S and length Z that is closed at both ends. The tube is initially filled with a volume $S \times z_{g,0}$ of gas and $S \times (Z - z_{g,0})$ of liquid (see Figure 3). Initially, the pressure $p_0 = p_{\text{ref}} = 1\,\text{bar}$ and temperature T_0 are uniform throughout the domain. Two initial temperatures $T_0 = 100\,\text{K}$ and $T_0 = 120\,\text{K}$ are considered that are respectively lower and higher than the saturation temperature $T_{\text{ref}} = T^{\text{sat}}(p_{\text{ref}}) = 111\,\text{K}$.

The gas and liquid phases follow respectively the ideal and stiffened gas equations of state, which are:

$$\rho_g(p,T) = \frac{p}{(\gamma_g - 1)\,\mathcal{C}_{v\,g} T}, \qquad \rho_l(p,T) = \frac{p + p_l^\infty}{(\gamma_l - 1)\,\mathcal{C}_{v\,l} T}, \tag{31a}$$

$$h_g(T) = \gamma_g \mathcal{C}_{v\,g}(T - T_{\text{ref}}) + \mathcal{L}, \qquad h_l(T) = \gamma_l \mathcal{C}_{v\,l}(T - T_{\text{ref}}), \tag{31b}$$

where ρ_k denotes the density of phase k ($k = g$ or l), $h_k = e_k + p/\rho_k$ its specific enthalpy, T_{ref} is a reference temperature and $\mathcal{L}$ the latent heat of the substance at T_{ref}. The values of the thermodynamical coefficients γ_k, p_k^∞ and $\mathcal{C}_{v\,k}$ used in this work are presented in Table 1.

The saturation pressure can be estimated using Clapeyron relation:

$$p^{\mathrm{sat}}(T) \simeq p_{\mathrm{ref}} \exp\left(\frac{\mathcal{L}}{(\gamma_g - 1)\,\mathcal{C}_{v\,g}}\left(\frac{1}{T_{\mathrm{ref}}} - \frac{1}{T}\right)\right), \tag{31c}$$

where $(p_{\mathrm{ref}}, T_{\mathrm{ref}})$ is a reference point on the saturation curve.

		Gas (g)	Liquid (l)
γ		1.4	3.3
p^∞	(Pa)	0	2.55×10^8
$\mathcal{C}_v$	($\mathrm{J{\cdot}kg^{-1}{\cdot}K^{-1}}$)	1500	2000
$\mathcal{L}$	($\mathrm{J{\cdot}kg^{-1}}$)	5×10^5	
p_{ref}	(Pa)	10^5	
T_{ref}	(K)	111	

Table 1: Thermodynamical coefficients used for the stiffened gas equation of state (31). These values roughly approximate the characteristics of methane at around 111 K and 1 bar.

A simplification of (30) will be used for the interfacial heat and mass flux. As in (14), the mass flow rate $J_{l\to g}$ will be written as a pressure difference in the form:

$$J_{l\to g} = -A\left(p_g - p^{\mathrm{sat}}(T_l)\right) \tag{32}$$

where A is a relaxation coefficient that is taken as constant with arbitrary value $A = 10^{-5}\,\mathrm{s\,m^{-1}}$.

4.2. Numerical diffusion only

For this first test case, no physical heat diffusion will be modeled. Only the numerical diffusion of the finite volume scheme will come into play. Its effect on the resolution will be illustrated by the used of several grids with different refinements.

The evolution of total gas mass and total entropy have been plotted in Figure 4 for the initial condition $T_0 = 100\,\mathrm{K}$. After a certain period of time the state of the system becomes stable: the total gas mass has diminished and the total entropy has grown. The final state is always a local equilibrium state at

the interface, as represented in Figure 5. However, this local equilibrium is the local equilibrium in one cell and depending of the size of the mesh, it will be a different state.

The temperature profile after the relaxation has been plotted is shown in Figure 6. Variation in the gas temperature is solely due to the variation in pressure caused by condensation. The temperature of the first liquid cell at the interface changes because of the latent heat released by condensation. Due to the kinetic relations (30), it is the temperature in this cell that set the liquid-vapor equilibrium ($T = T^{\mathrm{sat}}(p)$). The entropy condition imposes a heat flux such that the same cell receives the latent heat. Depending on the size of the cell, the temperature evolves differently for a given amount of energy.

This mesh dependent results can be interpreted as a dependence on heat diffusion, which appears here under the form of a numerical artifact. The need for physical thermal diffusion has been mentioned in Section 2. Otherwise, this limiting result might not be physical when the size of the cells goes to 0.

Figure 7 presents the evolution of the total mass of gas and of the total entropy for the initial condition $T_0 = 120\,\mathrm{K}$. The initial total mass of gas is lower than in the condensation case: since the initial temperature is different (and the pressure is the same), the initial gas density is different.

Although it is barely visible in Figure 7, the variation of total entropy is not strictly monotone. This can be explained by the numerous approximations that have been made to obtain the expressions for $J_{l\to g}$ and q.

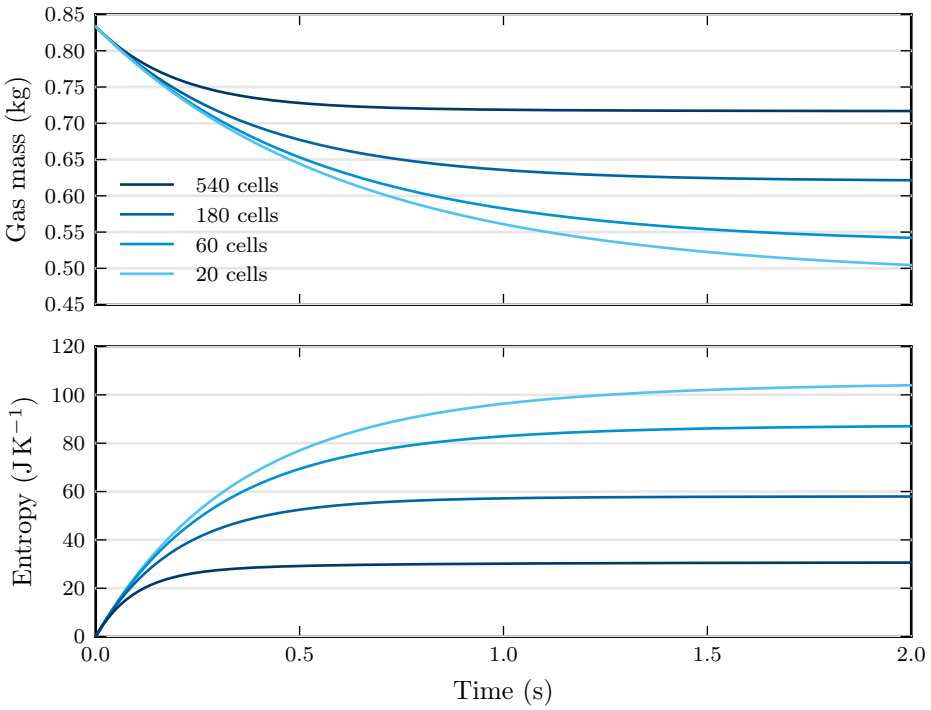

Figure 4: Evolution of the total mass of gas and of the total entropy as a function of time for the condensation test case ($T_0 = 100\,\mathrm{K}$) for various meshes.

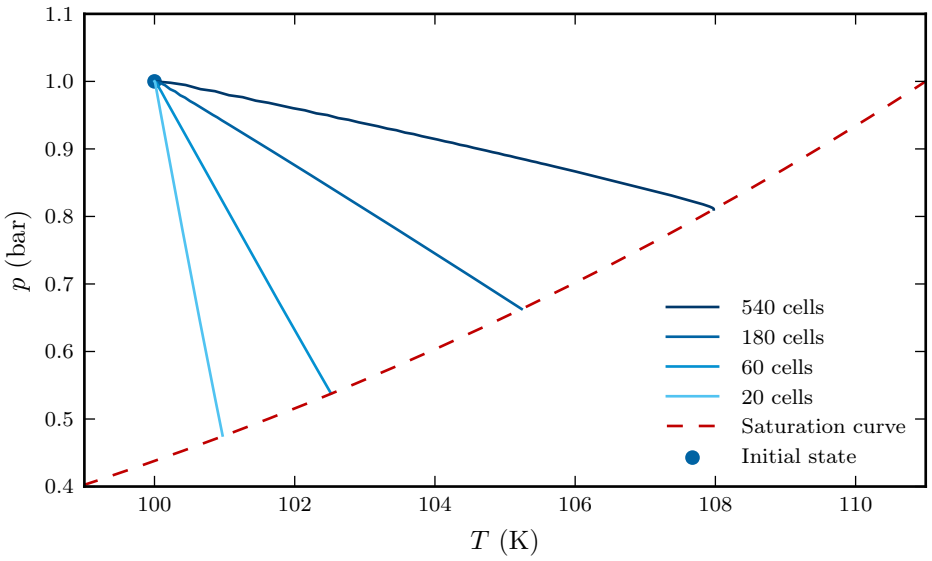

Figure 5: Evolution of the state of the first liquid cell at the left of interface in a (T, p) diagram for different mesh sizes.

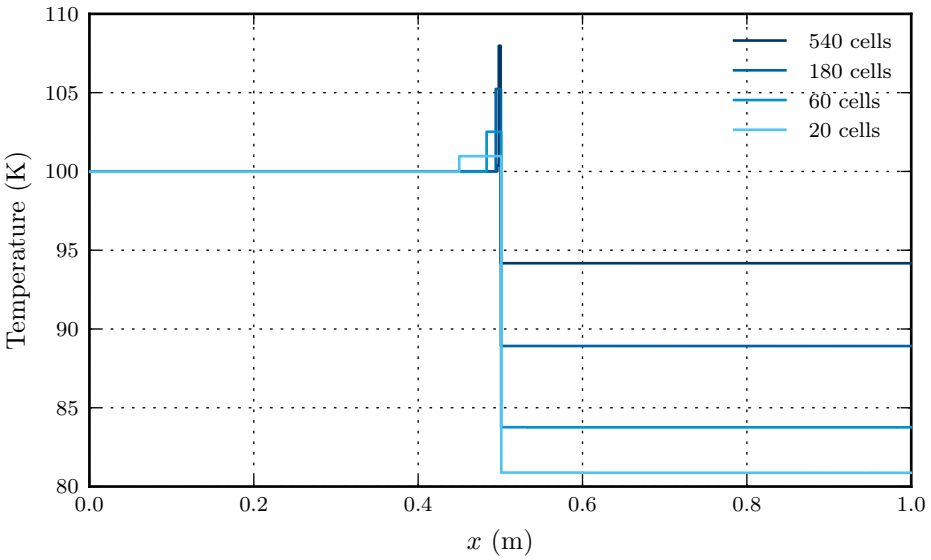

Figure 6: Temperature profile at the end of the simulation for the condensation test case ($T_0 = 100\,\mathrm{K}$) for various mesh sizes. The temperature of the gas on the right evolved due to the pressure variation. The released latent heat is in the first liquid cell at the interface.

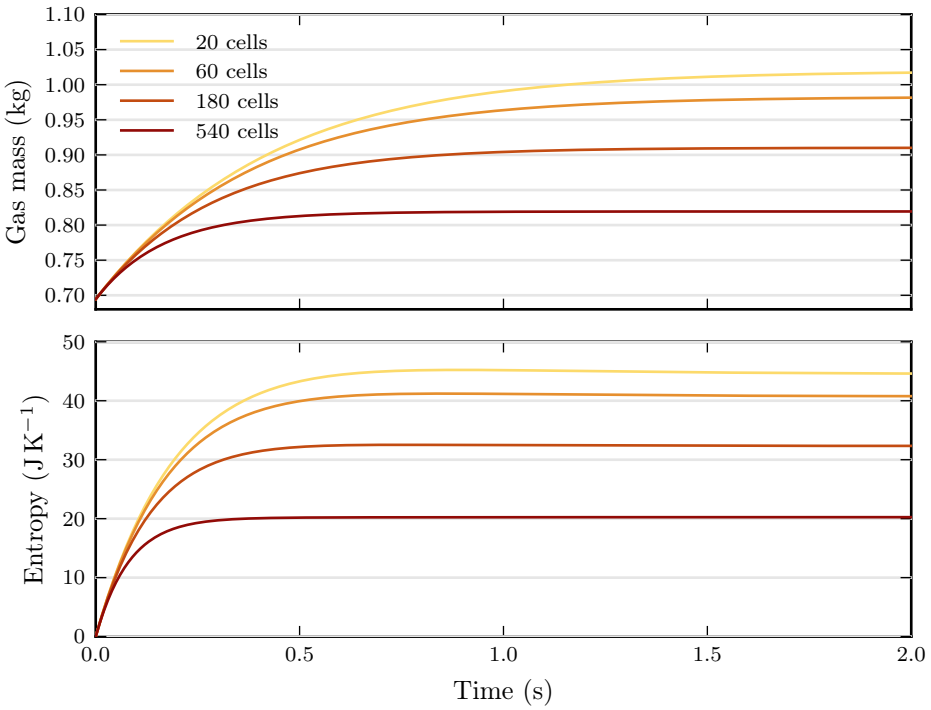

Figure 7: Evolution of the total gas mass and the total entropy as a function of time for the evaporation test case ($T_0 = 120\,\mathrm{K}$) for different mesh sizes.

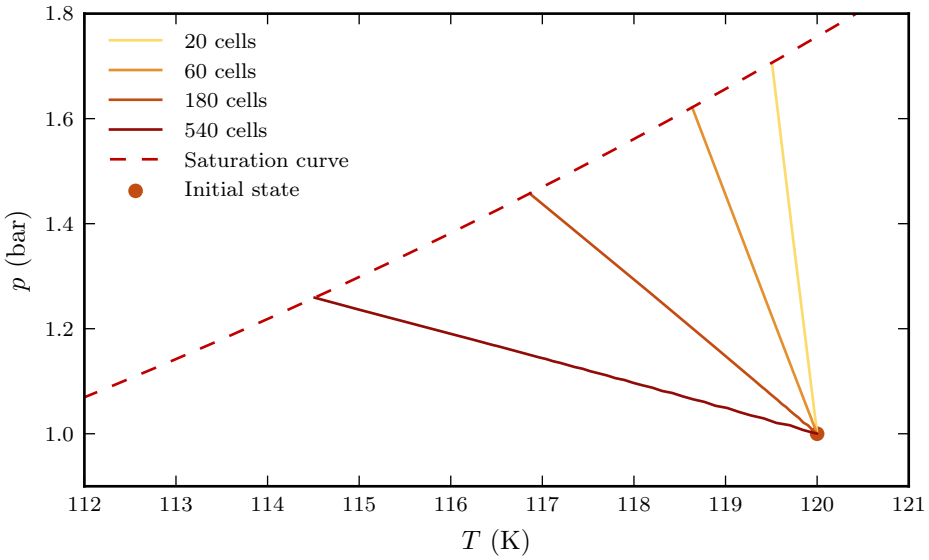

Figure 8: Evolution of the state of the first liquid cell to the left of the interface in the form of a (T, p) diagram for different mesh sizes.

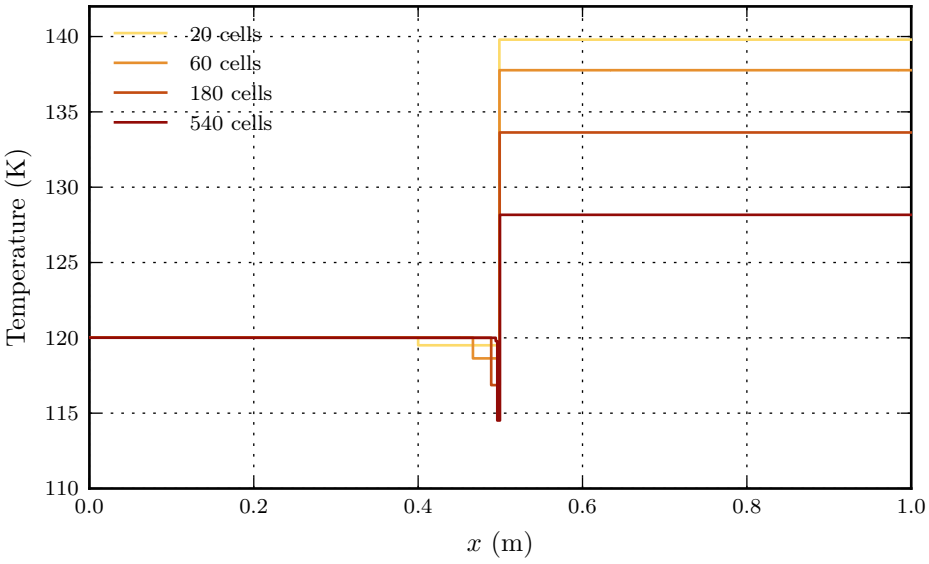

Figure 9: Profile of temperature at the end of the simulation for the evaporation test case ($T_0 = 120\,\mathrm{K}$) for different mesh sizes.

4.3. Convergence with thermal diffusion

Let us now introduce heat diffusion into our computations. The heat diffusion and the rest of the flux will be resolved separately using a time splitting approach.

The computation of the heat flux is carried out in two steps:

- First, taking β as the thermal diffusivity, the linear heat equation

  $$\partial_t T = \beta\, \partial_x^2 T,$$

  is discretized implicitly under the form

  $$T_j^{n+1,*} = T_j^n + \frac{\Delta t}{(\Delta x)^2}\left(-\beta_{j-1/2}\left(T_j^{n+1,*} - T_{j-1}^{n+1,*}\right) + \beta_{j+1/2}\left(T_{j+1}^{n+1,*} - T_j^{n+1,*}\right)\right).$$

  The temperature $T^{n+1,*}$ can be computed by solving a tridiagonal linear system.

- The evolution of T found by the previous formula may not respect the conservation of energy. Thus, the temperature field $T^{n+1,*}$ will be used to compute heat fluxes $q^{n+1,*}$,

  $$q_{j+1/2}^{n+1,*} = -\frac{k_{j+1/2}}{\Delta x}\left(T_{j+1}^{n+1,*} - T_j^{n+1,*}\right).$$

  where k is the heat conductivity. These fluxes can be used to compute new conservative variables:

  $$v_j^{n+1} = v_j^n + \frac{\Delta t}{\Delta x}\left(q_{j-1/2}^{n+1,*} - q_{j+1/2}^{n+1,*}\right).$$

We will now check the convergence of the solution when the mesh is refined and heat diffusion is present. For the sake of simplicity, the heat conductivity is the same in the gas and the liquid. Its value ($k = 10^2\,\mathrm{W\,m^{-1}\,K^{-1}}$) is high with regard to the physical values for water or methane, in order to easily distinguish the heat diffusion from the relatively high numerical diffusion. Actually, three time scales are involved in this problem: the time scale of the energy processing at the interface given by A, the time scale of the energy supply by physical

diffusion (set by k) and numerical diffusion (set by the mesh coarseness). In this paper, A has been kept constant, whereas k and the mesh coarseness vary.

In Figures 10 and 12, the evolution of total gas mass and of the total entropy is plotted as a function of time. This evolution can be decomposed into two phases:

- First a relaxation to local equilibrium at the interface, as observed in the results of the previous section.
- Then a steady state regime of phase change dominated by thermal conduction. The complete return toward global equilibrium in the domain is relatively long and has not been computed.

For the finest mesh sizes, small jumps can be seen in Figures 11 and 13, which are due to shifting of the condensate to the next cell in the scheme (see Figure 1). The cells used for the reconstruction are different when the interface moves from one cell to the next. For instance, for evaporation the condensate is one third liquid and two thirds gas at one step and it becomes two thirds liquid and one third gas by the next step. The inclusion of a new liquid cell (with a different temperature) slightly perturbs the evolution near the interface. However, this phenomenon is negligible and not visible on the evolution curves of Figures 10 and 12.

It does not appear for the coarser meshes because the total displacement of the interface is less than a single cell of the mesh. It is also expected to disapear when the size of the cell goes the zero: although the interface will more often reach a new cell, the quantitative effect of each perturbation should be lower. Using an higher order discretization could also attenuate this effect.

The convergence of the scheme can be checked on Figure 14. The error l_1 with respect to the finer mesh (3200 cells) is plotted as a function of the number of cells in the mesh. As expected for a first order scheme, all the curves have slopes in logarithmic scale between -0.9 and -1.1 (the dashed gray line is the reference line with slope -1). The error is lower for cases where the physical thermal diffusion is higher. A possible explanation is that the main source

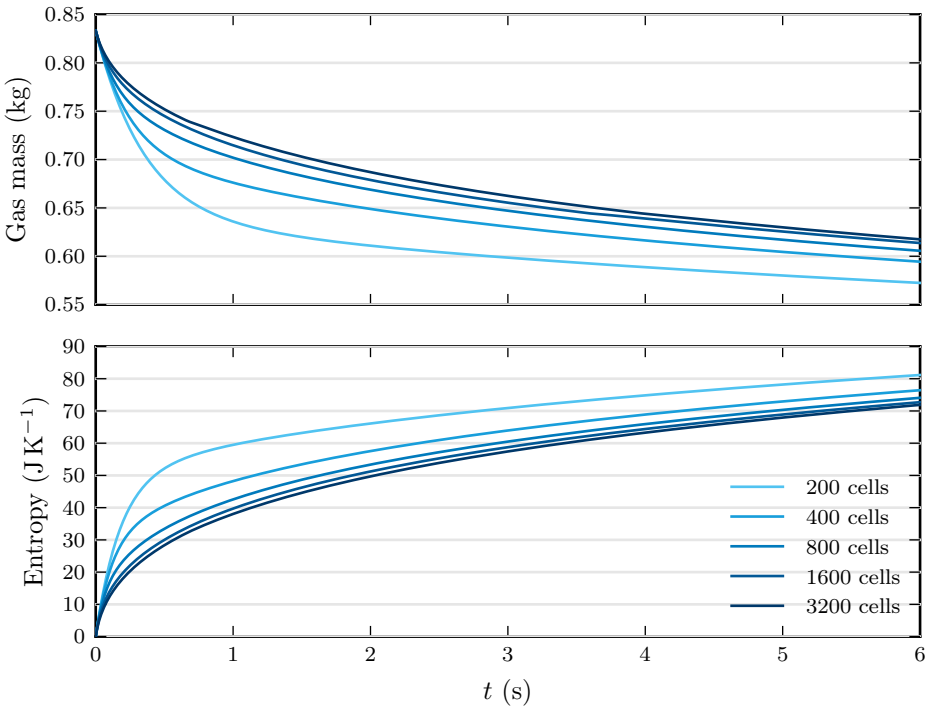

Figure 10: Evolution of the total gas mass and of the total entropy as functions of time for the condensation test case ($T_0 = 100\,\mathrm{K}$) for different mesh sizes, with heat diffusion.

of error is the numerical thermal diffusion and it is less significant when the physical thermal diffusion is higher.

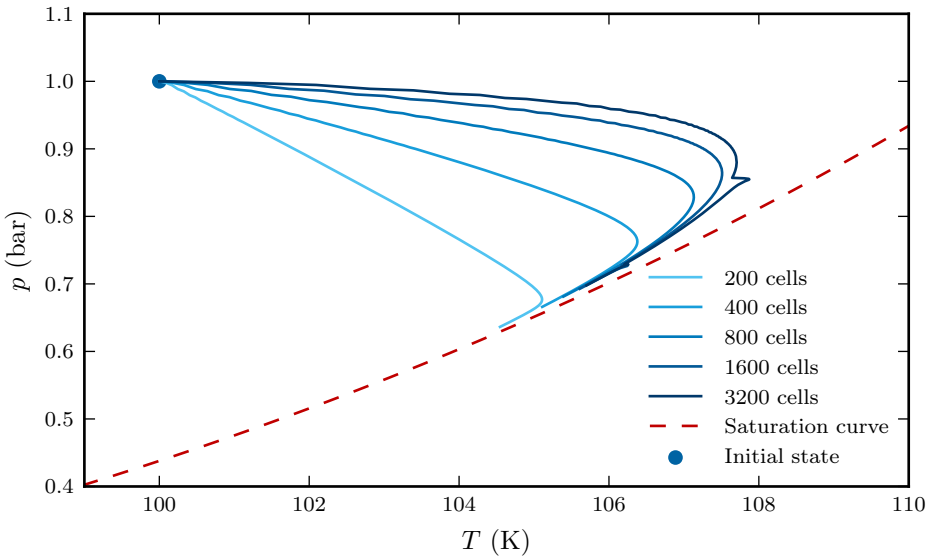

Figure 11: Evolution of the state of the first cell of liquid to the left of the interface in a (T, p) diagram in the condensation test case with heat diffusion for different mesh sizes.

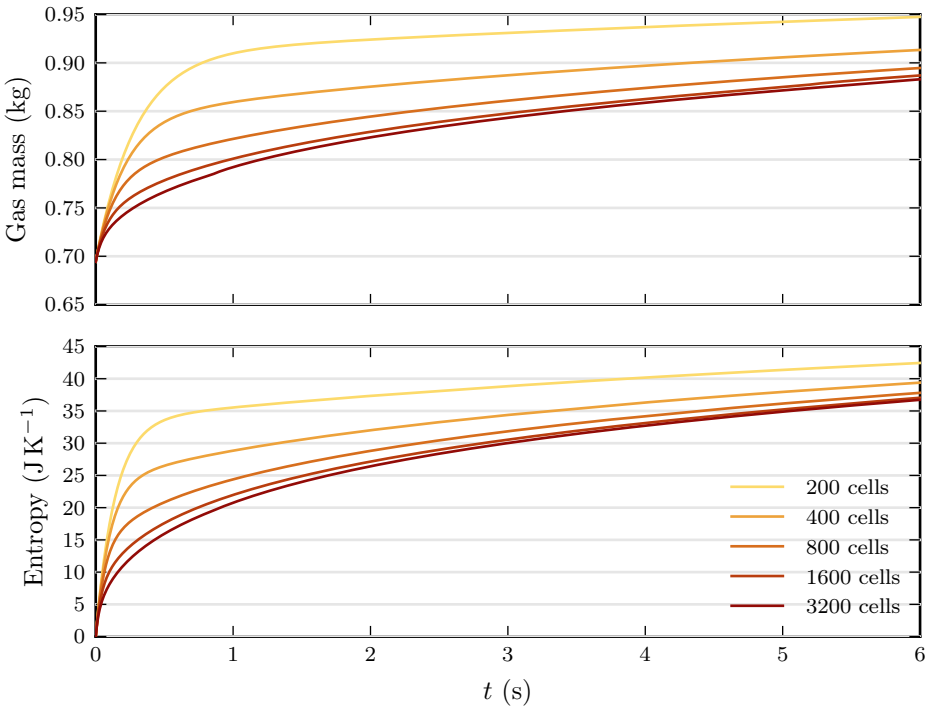

Figure 12: Evolution of the total gas mass and of the total entropy as functions of time for the evaporation test case ($T_0 = 120\,\mathrm{K}$) with heat diffusion for different mesh sizes.

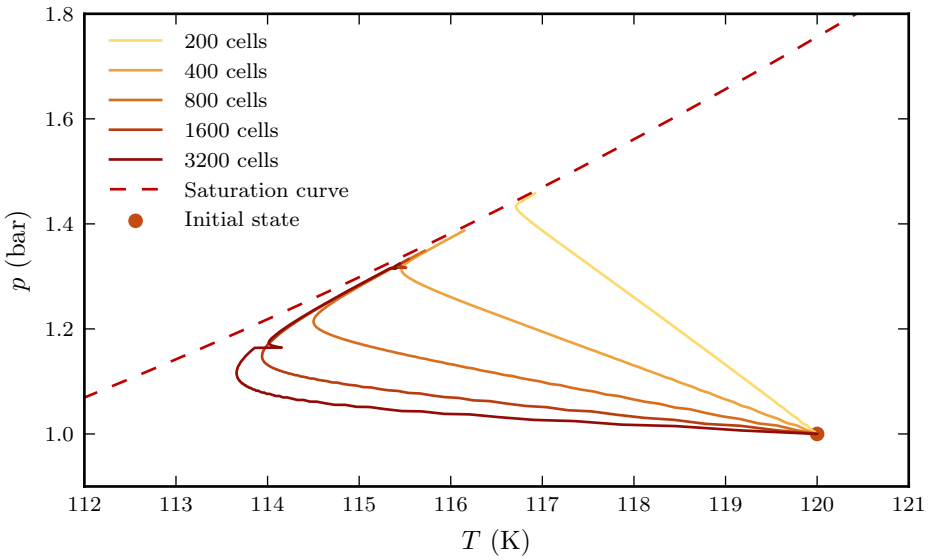

Figure 13: Evolution of the state of the first cell of liquid at the left of the interface in a (T, p) diagram in the evaporation test case with heat diffusion for different mesh sizes.

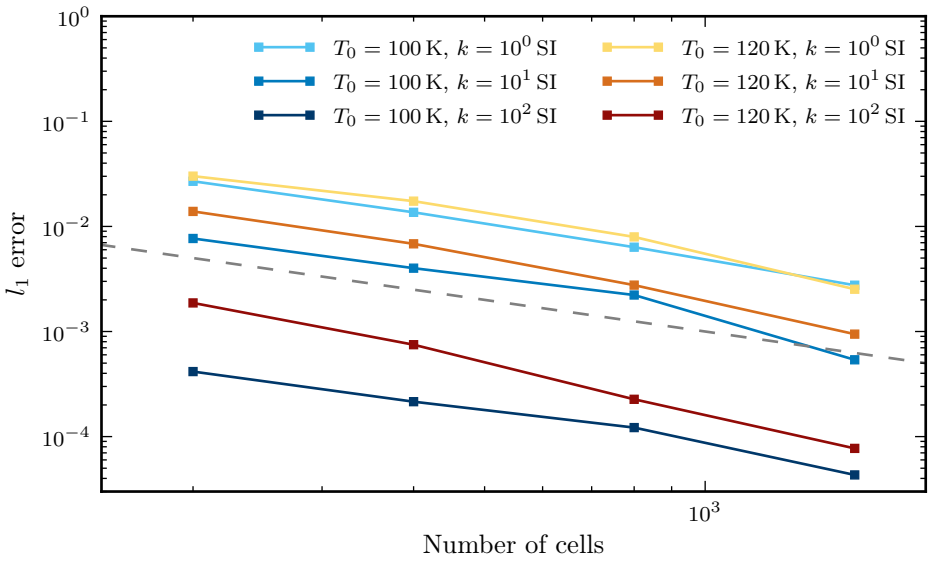

Figure 14: The l_1 error on the temperature profile at the end of the simulation as a function of the number of cells in the mesh in logarithmic scale. The error is computed with respect to the mesh with 3200 cells for the four coarser meshes between 200 and 1600 cells. The different curves correspond to different initial temperatures (condensation in shades of blue, evaporation in yellow and red) and different physical thermal diffusions. The dashed gray line is the $y = x^{-1}$ line, given as a reference.

4.4. Role of thermal conductivity

Finally, the influence of thermal conductivity k on relaxation towards the local equilibrium will be studied.

The mesh is made of 1600 cells. According to the previous results, this mesh does not correspond to a completely converged case. It is nonetheless sufficient to observe the influence of the physical thermal diffusion.

Results are presented in Figures 15, 16, 17 and 18. As already seen by studying the role of the numerical diffusion, a higher thermal diffusion leads to a higher phase change mass flow. The evolution of the thermodynamic state near the interface is closer to the isothermal return to equilibrium.

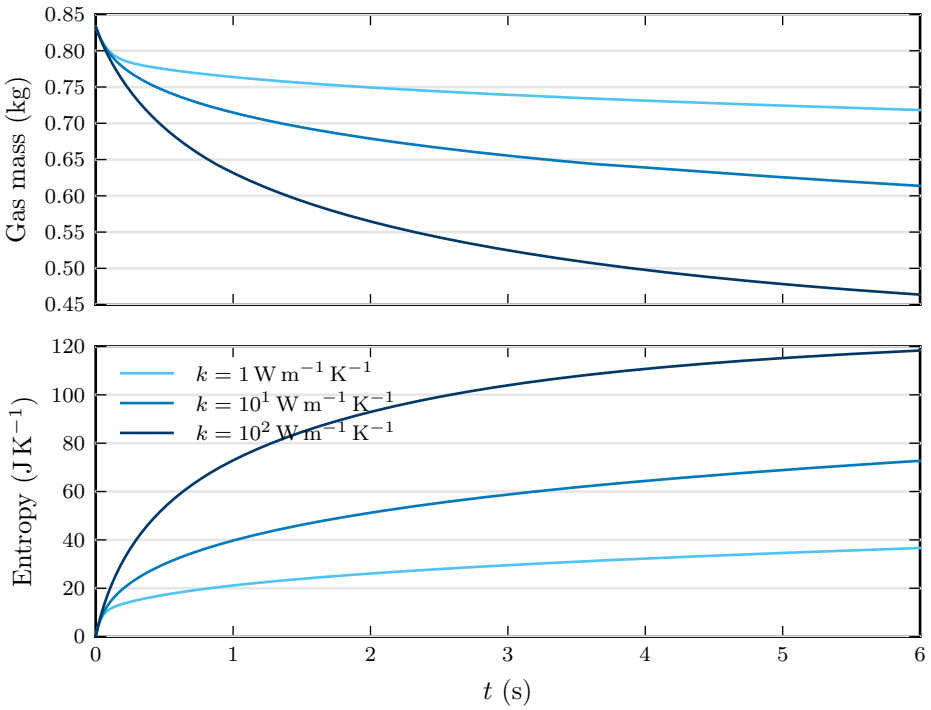

Figure 15: Evolution of the total gas mass and total entropy as a function of time for the condensation test case ($T_0 = 100\,\mathrm{K}$) for different thermal conductivities.

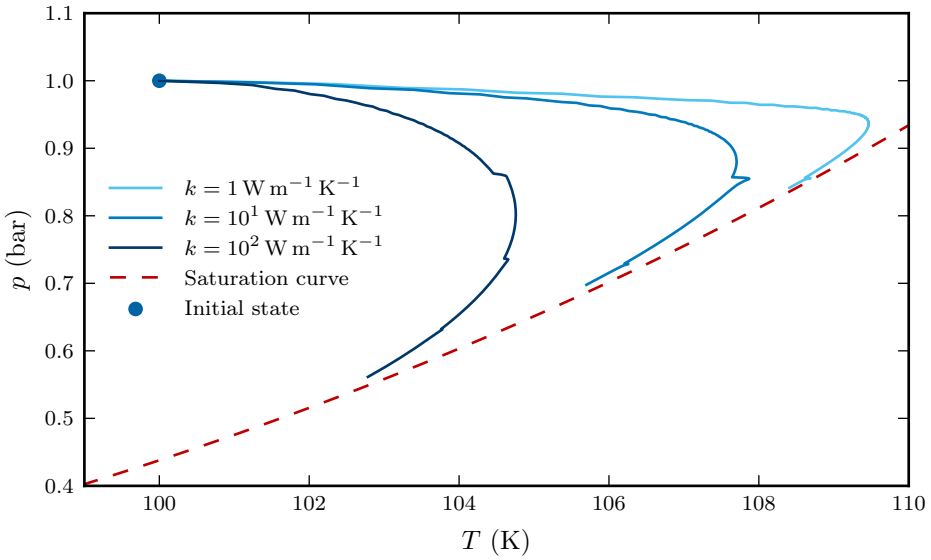

Figure 16: Condensation test case state evolution in the first cell of liquid to the left of the interface on a (T, p) diagram for different thermal conductivities.

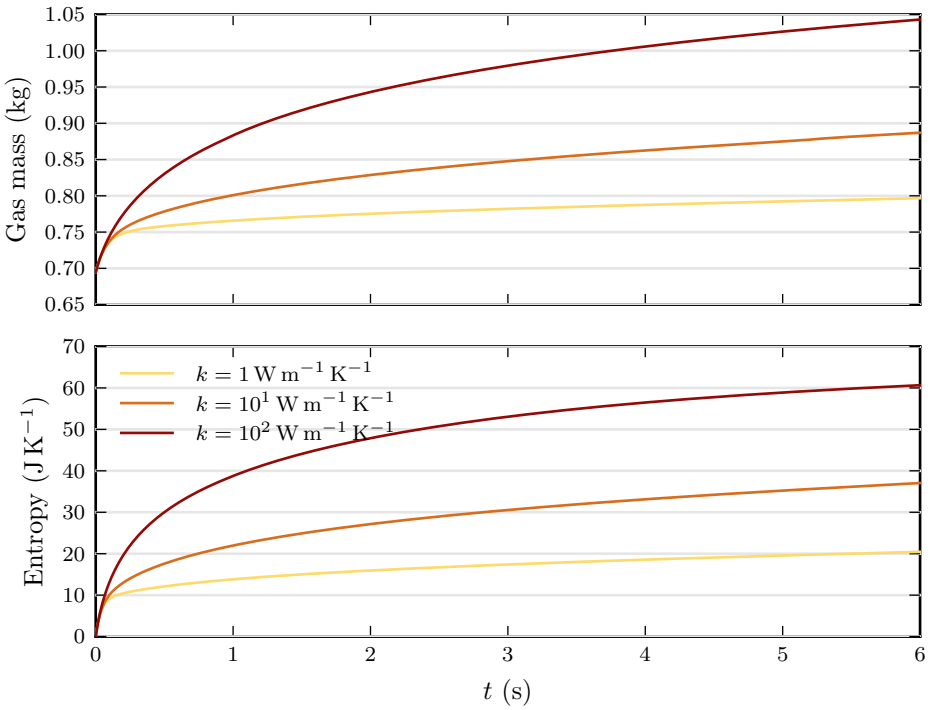

Figure 17: Evolution of the total gas mass and of the total entropy as functions of time in the evaporation test case ($T_0 = 120\,\mathrm{K}$) for different thermal conductivities.

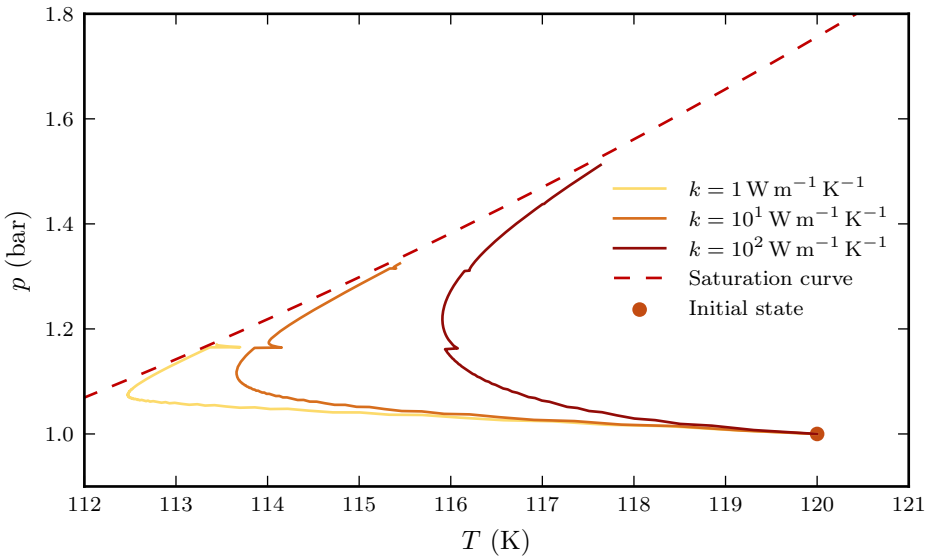

Figure 18: Evolution of the state of the first cell of liquid to the left of the interface on a (T, p) diagram in the evaporation test case for different thermal conductivities.

5. Application to a piston problem

In this last section, the model and its implementation will be applied to a simple problem, useful for the understanding of gas pocket impacts. This problem was first introduced by Bagnold in [36]. It has been studied in 0D with phase change in [32] and [16] as well as in 1D without phase change in [31]. The following is an extension of these works to 1D with phase change.

A few comparisons between the 0D and 1D models with phase change will first be presented. The purpose is to validate the numerical scheme presented above. More details on how various parameters relating to phase change influence the maximal pressure in the gas pocket can be found in [16] and [33].

5.1. Description

A schematic of the piston problem is shown in Figure 19. In a closed container, a piston with an initial velocity u_0 compresses a gas pocket and bounces on it.

In this paper the piston is simulated as a compressible liquid, though for the range of parameters considered the compressibility is almost negligible. The role of liquid compressibility has been discussed in [29] and [31].

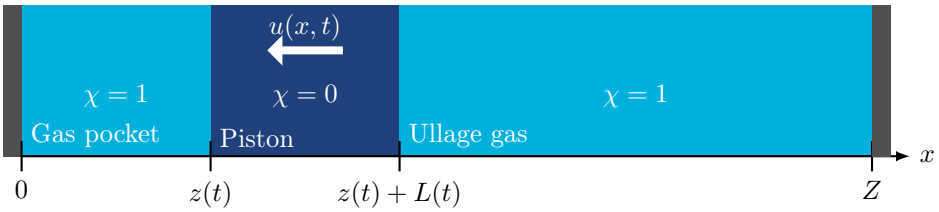

Figure 19: Schematic of the piston problem. Symbols z, L and Z are used to respectively denote the size of the gas pocket, the size of the piston and the total size of the domain, which is constant.

The initial conditions of the problem are:

$$z(t=0) = z_0, \qquad L(t=0) = L_0\,, \tag{33a}$$

$$\forall x \in [0, z_0], \quad \chi(x,0) = 1, \quad u(x,0) = u_0 \frac{x}{z_0}\,, \tag{33b}$$

$$\forall x \in [z_0, z_0 + L_0], \quad \chi(x,0) = 0, \quad u(x,0) = u_0, \tag{33c}$$

$$\forall x \in [z_0 + L_0, Z], \quad \chi(x,0) = 1, \quad u(x,0) = u_0 \frac{Z - x}{Z - z_0 - L_0}\,, \tag{33d}$$

and besides

$$\forall x \in [0, Z], \quad T(x,0) = T_0, \quad p(x,0) = p_0 = p^{\text{sat}}(T_0) \tag{33e}$$

Velocities have been chosen such that $u = u_0$ in the liquid, u is continuous at the liquid-gas interface and $u = 0$ at the walls. With the chosen orientation for the x axis, the compression of the gas pocket corresponds to $u_0 < 0$. We are interested in the pressure at the wall $p_{\text{wall}}(t) = p(x = 0, t)$.

The same equations of state (31) as in the previous test case are used. A dimensionless version of this problem with these equations of state has been presented in [16]. The main dimensionless magnitudes are the *impact number* S defined as

$$S = \frac{\rho_{l,0} L_0 u_0^2}{p_0 z_0}\,,$$

which describes the violence of the impact (see [31]), and Ω_m which is the inverse dimensionless time scale for relaxation towards liquid-vapor equilibrium, defined as

$$\Omega_m = G_m \frac{p_0}{\rho_{g,0}^2 T_0} \sqrt{\frac{\rho_{l,0} L_0}{p_0 z_0}}. \tag{34}$$

where G_m is the coefficient appearing in (30). When $\Omega_m \to 0$, phase change is too slow to have an influence on the compression of the gas pocket. On the other hand, when $\Omega_m \to \infty$, the local equilibrium at the interface is instantaneously reached.

Unlike the 0D model previously mentioned, the solution of this 1D piston problem is not necessarily periodic, even without mass exchange. Namely, the piston can act as a wave maker by sending pressure waves into the ullage gas and thus dispersing kinetic energy. This phenomenon has been described in more details in [16]. To avoid this damping of the oscillations, we will only consider geometries where the ullage gas pocket is relatively small.

Only phase change at the interface between the gas pocket and the piston will be taken into account. The mass flux between the piston and the ullage gas has been arbitrarily set to zero to make the comparison with the 0D model easier.

5.2. Numerical resolution

5.2.1. Isothermal problem

As mentioned in Section 4, the latent heat and its diffusion through thermal conduction plays an important role in the process of phase change. Since this phenomenon is purely 1D, it cannot really be reproduced by 0D surrogate models. Thus, we will first consider an isothermal evolution.

In Figure 20 several simulations of the pressure evolution at the wall are shown in an isothermal setting. The results of the present code are compared with the 0D extended Bagnold model of [16, 32] and the 1D problem solved with the isothermal diffuse interface model of [17]. There is a good match between the results. Note that the interface reconstruction scheme allows use of a coarser mesh than the diffuse interface method to achieve a similar level of accuracy.

5.2.2. Non-isothermal problem

Finally, we will discuss some non-isothermal results for the piston problem. In Figure 21, the evolution of the pressure at the wall has been plotted for several cases with the same impact number S and the same relaxation rate Ω_m. Both have been chosen to have relatively high values to observe the effect of phase change on the impact pressure. A much higher relaxation rate has led to instability in the numerical simulation: for this stiffer problem a more robust discretization of the equations should be investigated (e.g. implicit time discretization).

Dimensionless total heat capacity of the liquid layer was varied for the 0D Bagnold model with phase change: for an infinite heat capacity the temperature of the liquid is constant, while for a lower heat capacity the temperature of the liquid layer returns more easily to thermodynamical equilibrium. In the

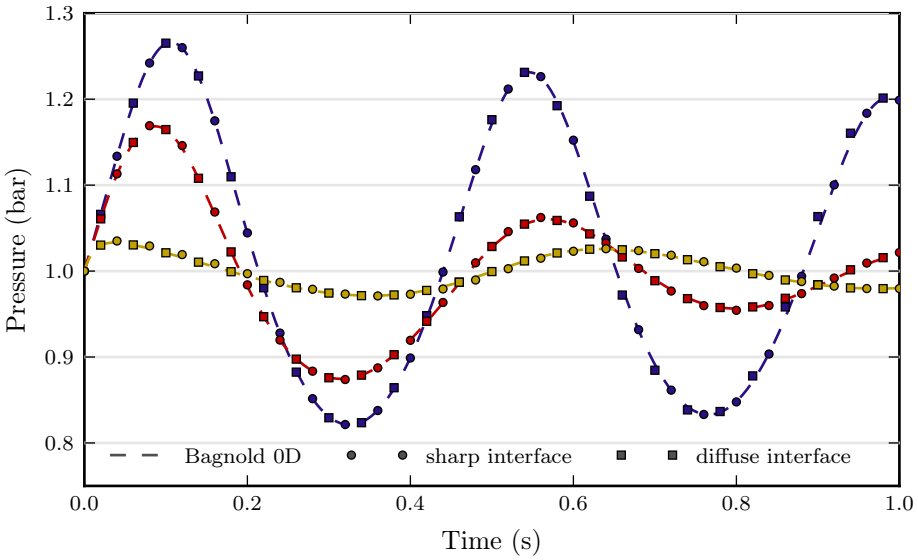

Figure 20: Evolution of the pressure at the wall p_{wall} as a function of time for 1D simulations for impact numbers $S = 10^{-1}$ and three different relaxation to equilibrium times Ω_m 10^{-1} (in blue) 1 (in red) and 10^{1} (in yellow) for an isothermal evolution. The dashed lines are the 0D Bagnold model [32], the round markers are for the present interface reconstruction scheme (mesh size: 150 cells), the square markers are the diffuse interface model from [17] (mesh size: 300 cells).

latter case, the exchanged mass that is necessary to retrieve the liquid-vapor equilibrium is lower and the effect of phase change on the pressure of the gas pocket is weaker.

The fineness of the mesh was varied for the 1D simulations of the present article. As we discussed in the previous section, this change can be seen as a change in the numerical thermal diffusion. For a finer mesh, the layer of liquid involved in phase change is thinner, which would equate to to a lower total heat capacity in the 0D model.

There are some similarities in the behavior of the 0D and 1D models, but there is never a perfect match, as is observed in the isothermal case. No 0D model can capture exactly the 1D thermal diffusion over several cells, as is

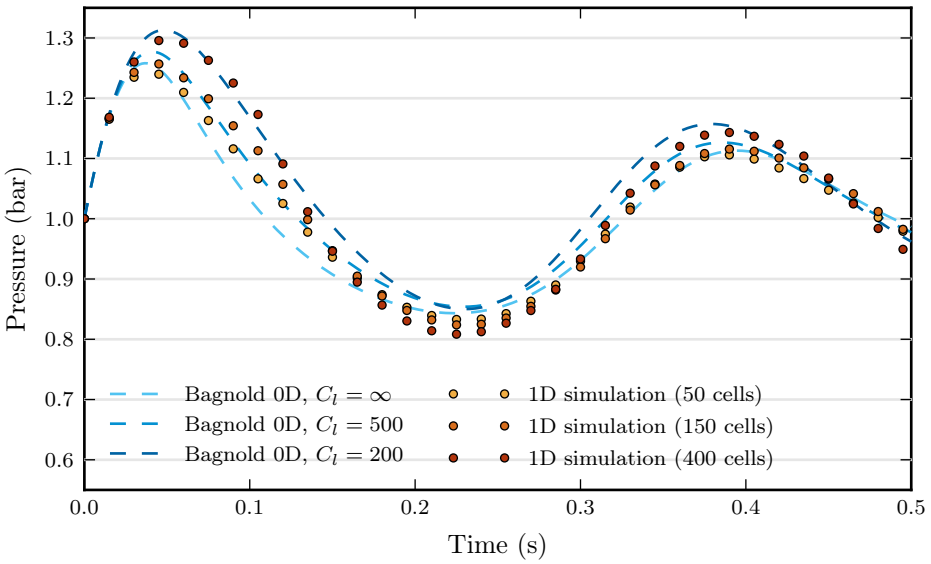

Figure 21: Evolution of the pressure p as a function of time for 1D simulations for impact numbers $S = 5 \cdot 10^{-1}$ and relaxation rate $\Omega_m = 2.3$ with the 0D Bagnold model (dashed line) and the 1D code (round markers). The 0D simulations have been computed for different dimensionless liquid thermal capacities between 200 and ∞ (the latter meaning isothermal liquid). The 1D simulations have been computed for several mesh sizes from 50 to 400 cells.

observed in 1D simulations.

In Figure 22, the profiles of pressure, density and velocity are shown during the compression of the gas pocket near the beginning of the simulation.

The pressure in the gas pocket is lower when phase change occurs, due to the condensation of some of the gas.

The density profiles with and without phase change are fairly similar. Phase change barely affects the shape of the piston: even the condensation of a large amount of gas does not significantly change the size of the piston. Moreover, at this early stage of the simulation, the position of the piston has not yet been affected by phase change.

Finally, note the velocity discontinuity at the gas pocket interface. Gas is absorbed by the piston as it moves forwards meaning that the velocity in the

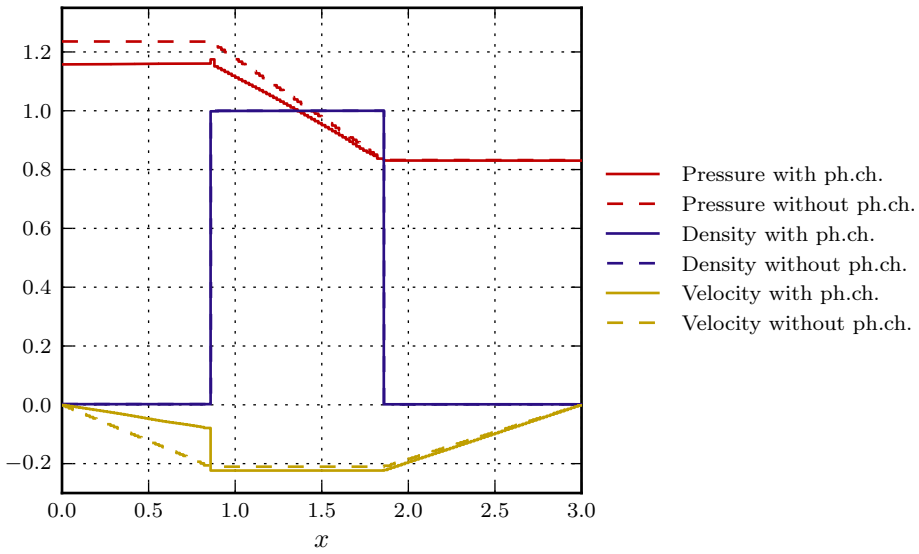

Figure 22: Profiles of dimensionless pressure, density and velocity during the compression of the gas pocket with phase change ($\Omega_m = 1$, plain lines) and without phase change ($\Omega_m = 0$, dashed lines) for a 150 cell mesh, $S = 10^{-1}$. The velocities are negative, while the piston is moving to the left and compressing the gas pocket on the left side of the domain.

gas pocket is lower in absolute value. No phase change occurs and the velocity profile is continuous for the liquid-vapor interface on the other side of the piston. The velocity of the piston is also slightly higher (in absolute value) in the case with phase change. Indeed the lower pressure in the gas pocket does not slow the piston down as mush as without phase change.

These results are expected and correspond to observations of the 0D models with phase change, as presented in [16, 32, 33].

6. Conclusion

In this paper, a model for two-separated-phase flow has been presented in a Lagrangian framework focusing on the interface. The evolution equations have been discretized and used with the interface reconstruction scheme of [1]. A

special focus has been placed on respecting the Second Principle of Thermodynamics.

Non-isothermal phase change depends on the thermal diffusion near the interface. In most of our cases, the numerical thermal diffusion is high with respect to the physical thermal diffusion. Phase change is thus artificially amplified. A similar bias appears due to the shape of the condensate near the interface. Small jumps in the phase change rate occur when the interface jumps from one cell to the next.

The thermal boundary layer at the interface is small with respect to the discretization of our domain. A possible improvement would be to model this boundary layer with more complex boundary conditions (11) at the liquid vapor interface. Then the numerical diffusion near the interface would not interfere as much with the thermodynamical relaxation.

Only a 1D scheme has been implemented and tested, but in principle there is no difficulty to extend the scheme to higher dimensions. The main challenge for higher dimensional simulations is the reconstruction of the interface, and this problem is independent of the phase change and has already been studied in [7] and [9]. The implementation of phase change in a 2D version of the scheme is the logical next step.

Another possible extension of the present work would be the modeling of nucleation. The appearance of new droplets or bubbles in pure phases could be modeled by the creation of new condensates in pure phase regions.

In the last section, results from the scheme have been compared with the results from the 0D Bagnold model with phase change found in [32] and [16]. The results match well, even if the 1D model does not behave exactly as the 0D model does from the point of view of thermal diffusion. When phase change is present, a reduction in the gas pocket pressure and a damping of the oscillations can be observed. This result is qualitatively in good accordance with the experimental results from [3]. However, for realistic wave impact problems, the thermal diffusion is very slow with respect to the characteristic time of the impact and thus only a very thin layer around the interface influences the phase

change. Thus the quantitative effect of phase change is expected to be very low. The role of the different parameters in the quantitative effect of phase change is further discussed in [33].

In this paper, as in other related work, we only studied a pure fluid. LNG is actually a mixture of several components: mostly methane, but also nitrogen, ethane and some heavier hydrocarbons. The thermodynamics of a mixture is more complex and so is the phase change modeling. When a condensible vapor turns into liquid, a layer of the other non-condensible gases can be left near the interface. This layer would isolate the rest of the condensible vapor from the liquid-vapor interface, thus slowing phase change. Thus, only a slow flow of condensible vapor, driven by molecular diffusion, would be able to change phase. This effect would complement the thermal boundary layer discussed in this paper and would present similar challenges.

7. Acknowledgment

This work was carried out during the Ph.D. degree studies of the first author, with the support of GTT and the Association Nationale de la Recherche et de la Technologie (ANRT) through *CIFRE* contract 2013/1301. The authors thank John Redford (CMLA) for proof-reading the article.

8. References

[1] J.-P. Braeunig, B. Desjardins, J.-M. Ghidaglia, A totally eulerian finite volume solver for multi-material fluid flows, European Journal of Mechanics - B/Fluids 28 (4) (2009) 475 – 485.

[2] E. Gervaise, P.-E. de Sèze, S. Maillard, Reliability-based methodology for sloshing assessment of membrane LNG vessels, in: Proc. of the 19th Int. Offshore and Polar Eng. Conf., Vol. 3, ISOPE, 2009, pp. 183–191.

[3] S. Maillard, L. Brosset, Influence of density ratio between liquid and gas on sloshing model test results, Int. J. of Offshore and Polar Eng. 19 (4) (2009) 271–279.

[4] J.-P. Braeunig, L. Brosset, F. Dias, J.-M. Ghidaglia, Phenomenological study of liquid impacts through 2d compressible two-fluid numerical simulations, in: Proc. of the 19th Int. Offshore and Polar Eng. Conf., Vol. 3, ISOPE, 2009, pp. 21–29.

[5] W. Lafeber, L. Brosset, H. Bogaert, Elementary loading processes (ELP) involved in breaking wave impacts: findings from the sloshel project, in: Proc. of the 22nd Int. Offshore and Polar Eng. Conf., Vol. 3, ISOPE, 2012, pp. 265–276.

[6] F. Dias, J.-M. Ghidaglia, Slamming: Recent progress in the evaluation of impact pressures, Annual Review of Fluid Mechanics 50 (2018) 243–273.

[7] J.-P. Braeunig, A pure eulerian method with interface capturing for multi-material fluid flows in dimension 1, 2 and 3, Ph.D. thesis, École normale supérieure de Cachan (2007).

[8] R. Loubère, J.-P. Braeunig, J.-M. Ghidaglia, A totally eulerian finite volume solver for multi-material fluid flows: Enhanced natural interface positioning (enip), European Journal of Mechanics-B/Fluids 31 (2012) 1–11.

[9] D. Chauveheid, Multimaterial and multiphysics flows: a colocated eulerian finite volume solver with interface capturing, analysis and simulations, Ph.D. thesis, École normale supérieure de Cachan (2012).

[10] J. Costes, Development of methods for resolving partial differential equations : from numerical scheme to simulation of industrial facilities, Ph.D. thesis, École normale supérieure de Cachan (2015).

[11] A. A. Mrabet, Algorithmic accelerations for wave impacts numerical simulation. Roofline type models for the performance characterization, application to CFD, Ph.D. thesis, École normale supérieure Paris-Saclay (2018).

[12] J. Costes, F. Dias, J.-M. Ghidaglia, A. A. Mrabet, Simulation of breaking wave impacts on a flat rigid wall by a 2d parallel finite volume solver

with two compressible fluids and an advanced free surface reconstruction, in: The Twenty-third International Offshore and Polar Engineering Conference, International Society of Offshore and Polar Engineers, 2013.

[13] J. Costes, J.-M. Ghidaglia, A. A. Mrabet, On the simulation of liquid impacts on a flat rigid wall by a 2d parallel finite volume solver, in: The Twenty-fourth International Ocean and Polar Engineering Conference, International Society of Offshore and Polar Engineers, 2014.

[14] P. Behruzi, M. Konopka, F. de Rose, G. Schwartz, Cryogenic slosh modeling in LNG ship tanks and spacecrafts, in: Proc. of the 24th Int. Offshore and Polar Eng. Conf., Vol. 3, ISOPE, 2014, pp. 209–217.

[15] P. Behruzi, D. Gaulke, D. Haake, L. Brosset, Modeling of impact waves in LNG ship tanks, Int. J. Offshore and Polar Eng. 27 (1) (2017) 18–26.

[16] M. Ancellin, Sur la modélisation physique et numérique du changement de phase interfacial lors d'impacts de vagues, Ph.D. thesis, École normale supérieure Paris-Saclay (2017).

[17] M. Ancellin, L. Brosset, J.-M. Ghidaglia, Numerical simulation of wave impacts with interfacial phase change: An isothermal averaged model, European Journal of Mechanics-B/Fluids 72 (2018) 631–644.

[18] J. G. Collier, J. R. Thome, Convective boiling and condensation, Clarendon Press, 1994.

[19] A. Faghri, Y. Zhang, Transport phenomena in multiphase systems, Elsevier, 2006.

[20] D. Jamet, O. Lebaigue, N. Coutris, J. M. Delhaye, The second gradient method for the direct numerical simulation of liquid–vapor flows with phase change, J. Comput. Phys. 169 (2) (2001) 624–651.

[21] D. Juric, G. Tryggvason, Computations of boiling flows, Int. J. Multiph. Flow 24 (3) (1998) 387–410.

[22] C. Kunkelmann, Numerical modeling and investigation of boiling phenomena, Ph.D. thesis (2011).

[23] M. Ishii, T. Hibiki, Thermo-fluid dynamics of two-phase flow, Springer New York, 2011.

[24] J. Stefan, Über die Theorie der Eisbildung, Monatshefte für Mathematik und Physik 1 (1) (1890-12-01) 1–6.

[25] S. De Groot, P. Mazur, Non-Equilibrium Thermodynamics, Dover Publications Inc., 1984.

[26] D. Bedeaux, L. J. F. Hermans, T. Ytrehus, Slow evaporation and condensation, Physica A: Statistical Mechanics and its Applications 169 (2) (1990) 263–280.

[27] D. Bedeaux, S. Kjelstrup, Irreversible thermodynamics—a tool to describe phase transitions far from global equilibrium, Chemical Engineering Science 59 (1) (2004) 109–118.

[28] D. Bedeaux, Non-equilibrium thermodynamics for engineers, World Scientific, 2010.

[29] M. Ancellin, L. Brosset, J.-M. Ghidaglia, Preliminary numerical results on the influence of phase change on wave impacts loads, in: Proc. of the 26th Int. Offshore and Polar Eng. Conf. (ISOPE 2016), Vol. 3, 2016, pp. 886–893.

[30] M. Ancellin, L. Brosset, J.-M. Ghidaglia, A hyperbolic model of nonequilibrium phase change at a sharp liquid–vapor interface, in: C. Klingenberg, M. Westdickenberg (Eds.), Theory, Numerics and Applications of Hyperbolic Problems I (Hyp2016), Springer International Publishing, Cham, 2018, pp. 59–69.

[31] L. Brosset, J.-M. Ghidaglia, P.-M. Guilcher, L. Le Tarnec, Generalized bagnold model, in: Proc. of the 23rd Int. Offshore and Polar Eng. Conf., Vol. 3, ISOPE, 2013, pp. 209–223.

[32] M. Ancellin, L. Brosset, J.-M. Ghidaglia, Influence of phase transition on sloshing impact pressures described by a generalized Bagnold's model, in: Proc. of the 22nd Int. Offshore and Polar Eng. Conf. (ISOPE 2012), Vol. 3, 2012, pp. 300–310.

[33] M. Ancellin, L. Brosset, J.-M. Ghidaglia, Numerical study of phase change influence on wave impact loads in LNG tanks on floating structures, in: Proc. of the 37th International Conference on Ocean, Offshore and Artic Engineering (OMAE2018), 2018.

[34] J. M. Delhaye, Jump conditions and entropy sources in two-phase systems. local instant formulation, International Journal of Multiphase Flow 1 (3) (1974) 395–409.

[35] J.-M. Ghidaglia, A. Kumbaro, G. Le Coq, On the numerical solution to two fluid models via a cell centered finite volume method, European Journal of Mechanics - B/Fluids 20 (6) (2001) 841–867.

[36] R. A. Bagnold, Interim techreport on wave-pressure research, Tech. rep., The Institution of Civil Enfineers (1939).